The Astrophysical Journal, 936:96 (7pp), 2022 September 10 https://doi.org/10.3847/1538-4357/ac8804

Accretion Disk Luminosity for Black Holes Surrounded by Dark Matter with Tangential Pressure

K. Boshkayev[1,2], T. Konysbayev[1,2], Ye. Kurmanov[1,2], O. Luongo[1,3,4], and D. Malafarina[5]
[1] National Nanotechnology Laboratory of Open Type, 050040 Almaty, Kazakhstan; kuantay@mail.ru, talgar_777@mail.ru, kurmanov.yergali@kaznu.kz, orlando.luongo@unicam.it
[2] Al-Farabi Kazakh National University, Al-Farabi ave. 71, 050040 Almaty, Kazakhstan
[3] Scuola di Scienze e Tecnologie, Università di Camerino, Via Madonna delle Carceri 9, Camerino, I-62032, Italy
[4] Dipartimento di Matematica, Università di Pisa, Largo B. Pontecorvo 5, Pisa, I-56127, Italy
[5] Department of Physics, Nazarbayev University, Kabanbay Batyr 53, 010000 Nur-Sultan, Kazakhstan; daniele.malafarina@nu.edu.kz
Received 2022 May 10; revised 2022 July 30; accepted 2022 August 9; published 2022 September 6

Abstract

We study the motion of test particles in the gravitational field of a Schwarzschild black hole surrounded by a spherical dark matter cloud with nonzero tangential pressure, and compute the luminosity of the accretion disk. The presence of nonvanishing tangential pressure allows us to mimic the dark matter's angular momentum, while still considering a static model, which simplifies the mathematical framework. We compare the numerical results of the influence of dark matter on the luminosity of the accretion disks around static supermassive black holes with the previously studied cases of isotropic and anisotropic pressures. We show that the flux and luminosity of the accretion disk in the presence of dark matter are different from the case of a Schwarzschild black hole in a vacuum, and highlight the impact of the presence of tangential pressures.

Unified Astronomy Thesaurus concepts: Black holes (162); Dark matter (353); Stellar accretion disks (1579); Schwarzschild black holes (1433); Dark matter distribution (356)

1. Introduction

It is widely agreed and supported by observations that the inner parts of large galaxies are characterized by the presence of supermassive compact objects (Pastorini et al. 2007; Davis et al. 2019), as massive as millions or even billions of solar masses. The most likely candidates for such objects are supermassive black holes (BHs), though extreme exotic compact objects are not excluded (Event Horizon Telescope Collaboration et al. 2019). While supermassive BHs are natural options for describing the objects residing at the galactic centers, their physical natures are currently not fully understood, however.

Indeed, current models for the origins of supermassive BHs are unable to predict the observed BH distribution in terms of mass and distance (Kormendy & Ho 2013). This poses a few cosmological issues: first, it is unclear how they have become so massive so quickly; and second, which cosmological epoch possessed the right conditions to favor their formation? Nevertheless, the spectroscopic properties of such supermassive BH candidates can be directly observed for several objects. In fact, we are able to study a wide number of supermassive BH candidates with masses in excess of one billion solar masses, located in the early universe (Volonteri 2010). From such observations, we can see that they behave as *accretors*, i.e., objects surrounded by accreting gas and material, forming disks and/or rotating substructures.

The accretion disk spectra have the great advantage of being easily detectable. It is therefore natural to look at the accretion disks in order to study the properties of the central objects (Biretta et al. 2002; Dokuchaev & Nazarova 2019). Also, as galaxies are immersed in dark matter (DM) halos, we expect that the BHs plus accretion disks must also be immersed in DM envelopes. Therefore, mathematical models of supermassive BHs surrounded by DM envelopes may be used to investigate the nature of the central object, as well as the properties of the proposed DM models.

To describe theoretically extreme compact objects, if we assume the validity of general relativity,[6] then the use of Einstein's field equations is essential, as one cannot avoid relativistic effects on the accretion disk luminosity. Consequently, the central object, responsible for the accretion disk's existence, produces a given geometry in its exterior. The simplest spacetime geometry is that of static BHs.

Nevertheless, if we wish to describe an accretion disk surrounding a Schwarzschild BH immersed in DM, we may choose a nonvacuum spherical solution for the exterior of the BH. In this case, a given energy–momentum tensor, whose equation of state can somehow be specified, must be provided. In this respect, the accretion disk luminosity can significantly change, due to the presence of different matter and pressure distributions outside the BH. Hence, different choices of the matter model or its equation of state can lead to different experimental signatures (Faber & Visser 2006).

In previous studies, we considered DM envelopes consisting of isotropic (Boshkayev et al. 2020) and anisotropic perfect fluids (Kurmanov et al. 2022). In this work, we shall focus on a static model for a DM envelope composed of counterrotating particles, the so-called "Einstein cluster" (Einstein 1939). Nonvanishing tangential pressures were introduced by Einstein as a way of describing a spherical and stationary configuration of collisionless particles rotating under their mutual gravitational attraction. Einstein's original "assumption that all particles move along

[6] For the sake of clarity, it is not imperative to consider Einstein's gravity, as many alternative theories have been proposed, and their implications may be tested with similar methods, as long as they fulfill the equivalence principle (Copeland et al. 2006; Capozziello et al. 2019).

circular paths around the center of symmetry of the cluster" implies a condition on the particles' geodesics, which, in turn, when extended to a continuous distribution of particles, determines the metric functions of the line element. In this sense, the metric mimics a cluster of rotating particles. The direction of motion must then be interpreted as opposite with respect to the tangential pressure, i.e., counterrotating. All particles on a given spherical shell r have the same angular momentum, leading the total angular momentum to vanish and the exterior metric to be static. The balance between gravity and the particles' centrifugal force keeps the system in equilibrium. The cluster is then formed by a continuous distribution of such shells between the center and the boundary. These assumptions were later extended to a dynamical contracting configuration by Kumar Datta (1970). The model is obtained from a Schwarzschild interior solution with nonvanishing tangential pressures, such as the one discussed in Florides (1974). Tangential pressures may be assumed to mimic the angular motion of the DM particles in the envelope. If such motion is slow enough with respect to the timescales of the massive particles in the accretion disk, the geometry of the DM envelope may be regarded as static (Kumar Datta 1970; Bondi 1971; Harada et al. 1998; Jhingan & Magli 2000).

In the description of the accretion disk, we assume that its mass is negligible, so that gas particles in the disk do not contribute to the geometry, which is uniquely determined by the BH and the DM profile. Further, we assume that the DM particles have a vanishing cross section of interaction with the normal baryonic matter in the disk, so that the motion of the test particles in the disk may be assumed to be geodesic.

Usually, DM models consider the DM particles to be in the form of dust, i.e., pressureless. In some cases, however, DM pressure may play a significant role—see, e.g., Faber & Visser (2006), Luongo & Muccino (2018), and Boshkayev et al. (2021a). Further, at a cosmological level, it has been argued that dark energy may emerge from DM pressure—see, e.g., Capozziello et al. (2018), Boshkayev et al. (2019, 2021b), and D'Agostino et al. (2022). In the model presented here, we do not consider radial pressure contributions, in the sense that we consider DM pressure small enough to be dust and the presence of tangential pressures to mimic the angular motion of the DM envelope.

To build the model, we follow the standard BH accretion theory developed in Novikov & Thorne (1973) and Page & Thorne (1974). We then evaluate the expected observational differences between the spectrum of a BH in a vacuum and that of a BH surrounded by a DM envelope. For this purpose, we compute the radiative flux and spectral luminosity of the accretion disk. In addition, we compare our findings with cases of nonvanishing isotropic and anisotropic pressures that were considered in earlier works (Boshkayev & Malafarina 2019; Boshkayev et al. 2020). We show that the luminosity of the accretion disks surrounding BHs immersed in DM is larger than that of BHs in a vacuum for a given BH mass, thus suggesting that the luminosity of the observed supermassive BHs may be explained by central objects with a smaller mass that are immersed in a DM envelope.

The paper is organized as follows. In Section 2, we describe the system and discuss the properties of the model. In Section 3, we define the radiative flux, spectral luminosity, and differential luminosity, while Section 4 is devoted to the numerical results for the spectral properties of the accretion disks. Finally, discussions about the potential implications of our model for astrophysical BH candidates are presented in Section 5. Throughout this paper, we use geometric units, setting $G = c = 1$.

2. Geometry of a Static BH Surrounded by a DM Profile

We consider here a general model for the inner region of a galaxy composed of a supermassive BH with a DM envelope surrounding it. In agreement with current observations, we assume DM not to interact with ordinary baryonic matter in the accretion disk, besides the gravitational interaction. To describe the physical properties of the system, we consider a spherically symmetric and static metric, written in the form

$$ds^2 = e^{N(r)}dt^2 - e^{\Lambda(r)}dr^2 - r^2(d\theta^2 + \sin^2\theta d\varphi^2), \qquad (1)$$

where we take (t, r, θ, φ) as the time and spherical coordinates, respectively. The relation of the energy–momentum tensor to the metric functions is obtained from Einstein's equations, and in the following we will restrict our attention to a DM cloud having only tangential pressures.

The introduction of the DM profile modifies the geometry around the BH with respect to the vacuum case. Therefore, our spacetime is made up of three parts, namely:

1. The galactic center is modeled by the Schwarzschild BH line element. Its mass, namely $M_{\rm BH}$, is a free parameter of our model, and its event horizon is located at $r_g = 2M_{\rm BH}$.
2. The BH's surrounding environment starts from an inner radius, namely $r_b > r_g$, up to the outer radius denoting the edge of the DM distribution, i.e., r_s. The DM mass is distributed inside this interval and its mass profile is $M_{\rm DM}(r)$.
3. Finally, at r_s, the DM distribution reaches its maximum value, and for $r > r_s$ we assume a vacuum, i.e., we consider a Schwarzschild exterior solution with a mass parameter given by $M_{\rm BH} + M_{\rm DM}(r_s)$, where $M_{\rm DM}(r_s)$ is the total DM mass.

By virtue of the above requirements, we can split the whole spacetime into three regions:

$$M(r) = \begin{cases} M_{\rm BH}, & r_g < r \leqslant r_b, \\ M_{\rm BH} + M_{\rm DM}(r), & r_b \leqslant r \leqslant r_s, \\ M_{\rm BH} + M_{\rm DM}(r_s), & r_s \leqslant r. \end{cases} \qquad (2)$$

Notice that unlike the case of DM with nonvanishing radial pressure, in the presence of only tangential pressure, the outer boundary of the DM cloud r_s is a free parameter.

The missing ingredient is clearly how the DM is distributed around the BH. Since we are not prescribing an equation of state, we have the freedom to choose the density profile for the DM envelope. In the following, we focus on two suitable phenomenological density distributions that are widely used in the literature. The first consists of a smooth exponential sphere density profile, given by

$$\rho_{\rm Exp}(r) = \rho_0 e^{-\frac{r}{r_0}}, \quad r \in [r_b, r_s], \qquad (3)$$

which was discussed as a DM candidate in Sofue (2013). Its slope seems to correctly agree with the experimental bounds inferred from the Milky Way and Andromeda galaxies. Its statistical soundness plays a key role in selecting it as a plausible candidate for modeling DM.

The second DM density distribution considered is the Burkert profile (Burkert 1995), which is given by

$$\rho_{\rm Bur}(r) = \frac{\rho_0}{\left(1 + \frac{r}{r_0}\right)\left(1 + \left(\frac{r}{r_0}\right)^2\right)}, \quad r \in [r_b, r_s]. \qquad (4)$$

The Burkert profile has the important advantage of not exhibiting a cusp singularity at the center $r = 0$, a problem that is present in several popular DM profiles for galaxies, such as, for example, the Navarro–Frenk–White profile (Navarro et al. 1996). In fact, the Navarro–Frenk–White and Burkert profiles are essentially analogous, except for the very inner region.

For both the density profiles considered, ρ_0 represents the DM density at $r = 0$, whereas r_0 is a scale radius, determined by observations.

Since, in general, for a spherical matter distribution, we have

$$M_{\rm DM}(r) = \int_{r_b}^{r} 4\pi\tilde{r}^2\rho(\tilde{r})\, d\tilde{r}, \tag{5}$$

for the exponential sphere and Burkert profiles, we obtain

$$M_{\rm DM}^{\rm Exp} = 8\pi r_0^3\rho_0\left[e^{-x_b}\left(1 + x_b + \frac{x_b^2}{2}\right) - \right.$$
$$\left. - e^{-x}\left(1 + x + \frac{x^2}{2}\right)\right], \tag{6}$$

$$M_{\rm DM}^{\rm Bur} = 2\pi r_0^3\rho_0\left[\frac{1}{2}\ln\left(\frac{(1+x)^2(1+x^2)}{(1+x_b)^2(1+x_b^2)}\right) + \right.$$
$$\left. + \arctan(x_b) - \arctan(x)\right], \tag{7}$$

with $x = r/r_0$ and $x_b = r_b/r_0$. For vanishing r_b, Equation (6) reduces to the one obtained in Sofue (2013).

The components of the energy–momentum tensor in the absence of radial pressures can be obtained following Florides (1974) as

$$T_0^0 = \rho(r), \quad T_1^1 = 0, \tag{8a}$$

$$T_2^2 = T_3^3 = -\frac{\rho(r)M(r)}{2(r - 2M(r))}. \tag{8b}$$

Using Einstein's equations with the line element of Equation (1), we obtain the following expressions for the metric function inside the DM envelope:

$$e^{-\Lambda(r)} = 1 - \frac{2M(r)}{r}, \tag{9a}$$

$$\frac{dN(r)}{dr} = \frac{2M(r)}{r(r - 2M(r))}, \tag{9b}$$

which completely determine the geometry once $M(r)$ is given. The details of the derivations of the field equations are discussed in the Appendix.

Since the spacetime is divided into three parts, we need to consider the matching between the different regions at the boundaries. The inner and outer regions are vacuum solutions, while the region in between contains the DM distribution. The values of the density and metric functions at the inner boundary r_b are $\rho(r_b)$, $N(r_b)$, and $\Lambda(r_b)$, and similarly for the outer boundary r_s. The boundary densities can be immediately computed from Equations (3) and (4), respectively, as $\rho(r_b) = \rho_b$, while $N(r_b)$ is valid for both profiles and reads

$$N(r_b) = N_b = \ln\left(1 - \frac{r_g}{r_b}\right) + C, \tag{10}$$

where C is a constant, unknown a priori, determined by the demand that $N(r)$ be continuous across the boundary. This requirement, namely that g_{tt} is continuous at the boundary, together with the continuity of the rest of the metric tensor components, are the only necessary conditions for fulfilling the Israel matching conditions (Israel 1966, 1967). Consequently, the metric functions, $N(r)$ and $\Lambda(r)$, are evaluated as

$$e^{N(r)} = \begin{cases} \left(1 - \dfrac{r_g}{r}\right)\tilde{C}, & r_g < r \leqslant r_b, \\ e^{N(r)}, & r_b \leqslant r \leqslant r_s, \\ 1 - \dfrac{2M(r_s)}{r}, & r_s \leqslant r, \end{cases} \tag{11}$$

where $\tilde{C} = e^C$ and $N(r)$ in the DM region is the solution of Equation (9b) that fulfills the boundary conditions, and

$$e^{\Lambda(r)} = \begin{cases} \left(1 - \dfrac{r_g}{r}\right)^{-1}, & r_g < r \leqslant r_b, \\ \left(1 - \dfrac{2M(r)}{r}\right)^{-1}, & r_b \leqslant r \leqslant r_s, \\ \left(1 - \dfrac{2M(r_s)}{r}\right)^{-1}, & r_s \leqslant r. \end{cases} \tag{12}$$

So, once the mass profile is known, $\Lambda(r)$ is also known. Since the mass profile is determined unambiguously from Equation (5) and, consequently, Equations (6)–(7), defining $\Lambda(r)$, one has to numerically solve Equation (9b) to infer $N(r)$. The integration is carried out from r_b to r_s, and the integration constant is defined from Equation (11), when $r = r_s$. C is then determined from the numerical solution of Equation (9b), when $r = r_b$. Note that since the region $r < r_b$ is not relevant for our purposes, it is not necessary to explicitly evaluate C, which can then be absorbed into the usual Schwarzschild form by a redefinition of t in the inner region.

3. Radiative Flux and Spectral Luminosity of the Accretion Disk

In this section, we investigate the flux and spectral luminosity of the accretion disk, following the framework proposed by Novikov & Thorne (1973) and Page & Thorne (1974).

First, we focus on the angular velocity, angular momentum, and energy of the particles in the disk. Denoting g as the metric determinant of the three-dimensional subspace, composed of the set t, r, φ, we have $\sqrt{g} = \sqrt{g_{tt}g_{rr}g_{\varphi\varphi}}$. So, one can write

$$\Omega(r) = \frac{d\varphi}{dt} = \sqrt{-\frac{\partial_r g_{tt}}{\partial_r g_{\varphi\varphi}}}, \tag{13}$$

$$L(r) = -u_\varphi = -u^\varphi g_{\varphi\varphi} = -\Omega u^t g_{\varphi\varphi}, \tag{14}$$

and

$$E(r) = u_t = u^t g_{tt}, \tag{15}$$

$$u^t(r) = \dot{t} = \frac{1}{\sqrt{g_{tt} + \Omega^2 g_{\varphi\varphi}}}, \tag{16}$$

where $\Omega = \Omega(r)$ is the orbital angular velocity, $L = L(r)$ is the orbital angular momentum per unit mass, $E = E(r)$ is the energy per unit mass of the test particle, and u^μ is the particle's four velocity.

To implement the above in the numerical setup, it is helpful to define dimensionless counterparts to the above quantities. Thus, denoting the dimensionless quantities with the superscript *, we define

$$\Omega^{*}(r) = M_T \Omega(r), \tag{17a}$$

$$L^{*}(r) = \frac{L(r)}{M_T}, \tag{17b}$$

$$E^{*}(r) = E(r), \tag{17c}$$

$$\mathcal{F}^{*}(r) = M_T^2 \mathcal{F}(r), \tag{17d}$$

where M_T is the total mass of the system, which corresponds to $M_T = M_{\rm BH} + M(r_s)$, for the case of a BH with DM distribution, and to $M_T = M_{\rm BH}$, for the case of a BH in a vacuum, i.e., without DM.

The radiative flux, $\mathcal{F}$, emitted from the disk is defined as

$$\mathcal{F}(r) = -\frac{\dot{m}}{4\pi\sqrt{g}} \frac{\Omega_{,r}}{(E - \Omega L)^2} \int_{r_{\rm ISCO}}^{r} (E - \Omega L) L_{,\tilde{r}} d\tilde{r}, \tag{18}$$

which clearly depends on the quantity $\dot{m}$, namely the disk's mass accretion rate, which, while being an essential ingredient in the computation, is also a rather arbitrary quantity. The simplest approach is to take it as a constant. Notice that $\mathcal{F}$ is not an observable quantity, and therefore we must use it to build some quantity that can be measured. Once $\dot{m}$ has been fixed, we can construct another important quantity, namely the differential luminosity at infinity $\mathcal{L}_\infty$, which is physically interpreted as the energy per unit time reaching an observer at infinity. Following Novikov & Thorne (1973) and Page & Thorne (1974), we have

$$\frac{d\mathcal{L}_\infty}{d\ln r} = 4\pi r \sqrt{g} E \mathcal{F}(r). \tag{19}$$

Now, in order to obtain a spectral luminosity, as a function of the radiation frequency ν, we need to choose an emission profile for the disk. The simplest approach consists of approximating the emission with that of a blackbody. We can then convert the differential luminosity as a function of r into the spectral luminosity, which depends on the frequency ν, via (Boshkayev et al. 2020)

$$\nu\mathcal{L}_{\nu,\infty} = \frac{60}{\pi^3} \int_{r_{\rm ISCO}}^{\infty} \frac{\sqrt{g} E}{M_T^2} \frac{(u^t y)^4}{\exp[u^t y/\mathcal{F}^{*1/4}] - 1} dr, \tag{20}$$

where we set the dimensionless variable $y = h\nu/kT_*$, with h being the Planck constant, k being the Boltzmann constant, and T_* being the characteristic temperature defined from the Stefan–Boltzmann law, namely

$$\sigma T_* = \frac{\dot{m}}{4\pi M_T^2}, \tag{21}$$

with σ being the Stefan–Boltzmann constant.

4. Numerical Results

To obtain numerical results, we need to set the free parameters of the model. Bearing in mind the qualitative description of the environment surrounding supermassive BHs, we set

$$M_{\rm BH} = 5 \times 10^8 M_\odot \approx 4.933 \text{ au}, \tag{22a}$$

$$r_b = \frac{11 M_{\rm BH}}{2} \approx 27.133 \text{ au}, \tag{22b}$$

$$r_0 = 10 \text{ au}, \tag{22c}$$

$$\rho_0^* = \rho_0 \times (10^5 \text{ au}^2), \tag{22d}$$

where $M_\odot$ is the Sun's mass, r_b is the inner boundary where the DM distribution starts, and ρ_0 remains a free parameter that we can vary. The value of $M_{\rm BH}$ is chosen within the range of astrophysical supermassive BHs that are observed with masses from a few million to several billion times the mass of the Sun. The values of r_b and r_0 determine the inner boundary and extent of the DM distribution, and they are fixed in such a way that the DM envelope's inner boundary is smaller than the ISCO radius for the Schwarzschild BH and the concentration of DM remains close to the central BH, since r_0 determines the slope of the exponential density profile. Finally, the value of ρ_0 is chosen to be within the estimates for the density of the DM at the galactic center, which range from $\sim 10^{14}$ to $\sim 10^{23} M_\odot$ pc^{-3}, as shown by Argüelles et al. (2018, 2019). In the following, the value of the DM density parameter ρ_0^* is chosen to be $\{0.5, 1, 1.5, 2\}$. Note that 1 au$^{-2} \approx$ 60.173 cm$^{-3} \approx$ $8.9 \times 10^{23} M_\odot$pc^{-3}.

The metric functions in the DM envelope are obtained by numerically solving Equation (9b) with the appropriate boundary conditions. We then calculate the orbital parameters of the test particles in the accretion disk and the spectral properties of the disk's emission, and compare the results with the case of a BH in a vacuum and a BH surrounded by other kinds of DM profiles.

In Figure 1, we plot the angular velocity and angular momentum (the left and right panels, respectively) of the test particles in the accretion disk. In the figure, the DM density profile is the exponential sphere given by Equation (3), and, for comparison, we show the corresponding curves for test particles around a BH in a vacuum, given by $\rho_0^* = 0$. Noticeably, the curves of the angular velocity in the presence of DM lie below the pure vacuum case at all ranges of radius, while the curves of orbital angular momentum lie below the vacuum case at small radii and at large radii.

The angular momentum is important, since, by solving the equation $dL/dr = 0$, one obtains the smallest radius where stable circular orbits are allowed to exist, namely $r_{\rm ISCO}$, which determines the inner edge of the accretion disk. The inner edge of the disk in turn appears in the integral of Equation (18), and therefore is related to observable quantities.

In Figure 2, we plot the dimensionless energy of the test particles in the accretion disk (left panel) and the dimensionless radiative flux (right panel), given in Equation (18), emitted by the accretion disk as a function of the dimensionless radial coordinate r/M_T. For small values of r/M_T, the energy of the test particles is smaller in the presence of DM with respect to a BH in a vacuum, but for larger r/M_T, the energy is larger than it is in a vacuum. On the other hand, one can observe that the dimensionless radiative flux in the presence of DM is always larger than the pure vacuum case for any r/M_T.

In Figure 3, we plot the differential luminosity (left panel) as a function of r/M_T and the spectral luminosity (right panel) of the accretion disk as a function of $h\nu/kT_*$. Again, for all values of r/M_T, the differential luminosity is larger in the presence of DM with respect to the vacuum case. Though all the quantities, i.e., Ω, L, E, $\mathcal{F}$, and $rd\mathcal{L}_\infty/dr$, are crucial and present theoretical interest, the quantity that may be measured through observation is the spectral luminosity.

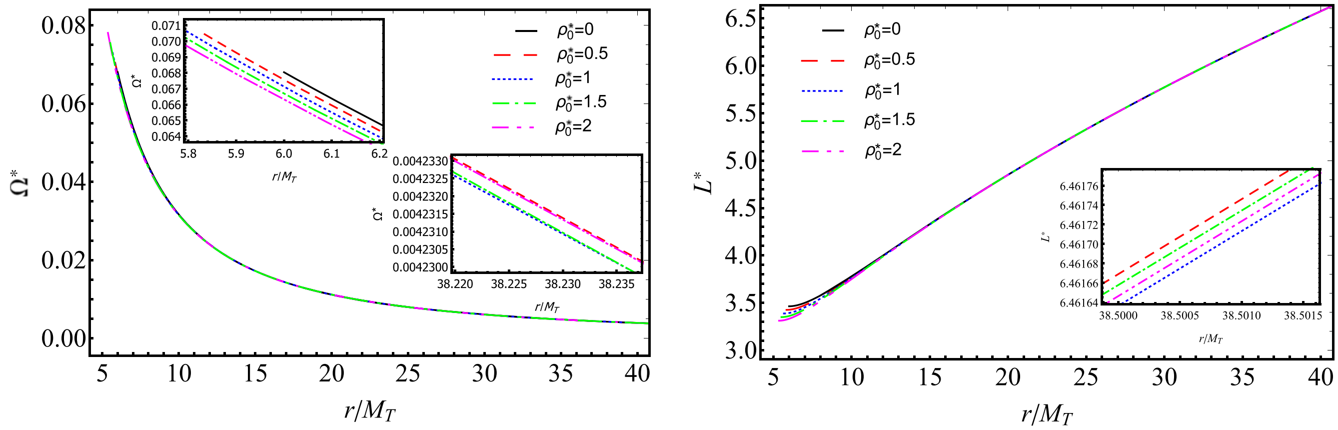

Figure 1. Numerical evaluation of the orbital parameters of the test particles in the accretion disk in the presence of the exponential sphere DM profile as functions of r/M_T. Left: orbital angular velocity Ω^*. Right: orbital angular momentum L^*. In both figures, the solid curves represent the case of a static BH without DM and the dashed curves show the presence of DM with different values of $\rho_0^* = \rho_0/(10^{-5}\,\mathrm{au}^{-2})$. The corresponding plots for the Burkert density profile can also be obtained and do not show qualitative differences.

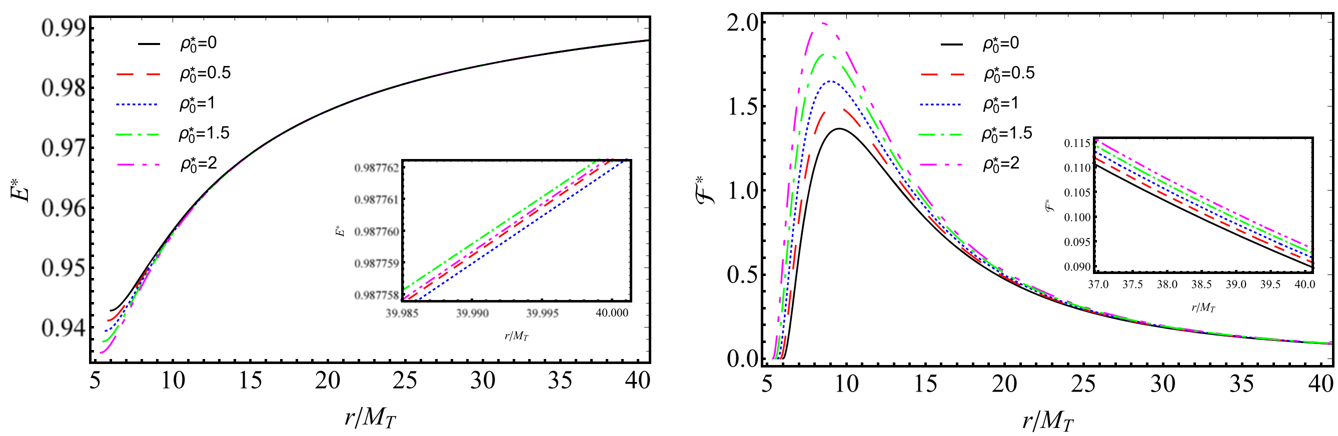

Figure 2. Left: energy of the test particles E^* in the accretion disk of a BH surrounded by DM as a function of the dimensionless radial coordinate r/M_T. Right: radiative flux $\mathcal{F}^*$, divided by 10^{-5}, emitted by the accretion disk as a function of r/M_T. In both figures, the solid curves represent the case of a static BH without DM and the dashed curves show the presence of DM with different $\rho_0^* = \rho_0/(10^{-5}\,\mathrm{au}^{-2})$. The plots correspond to the exponential sphere density profile. The corresponding plots for the Burkert density profile can also be obtained and do not show qualitative differences.

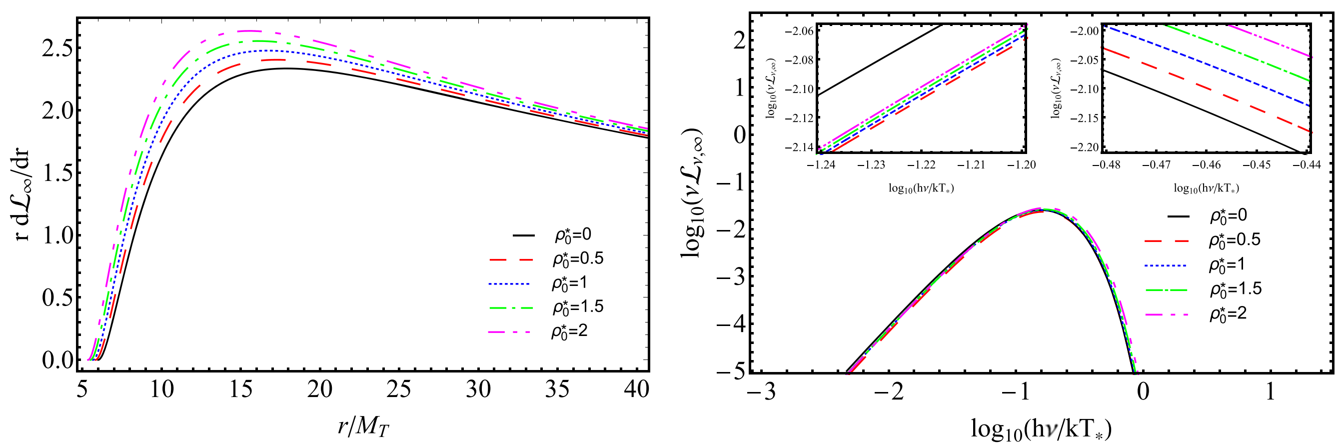

Figure 3. Left: numerical evaluation of the differential luminosity scaled in powers of 10^{-2} as a function of r/M_T. Right panel: numerical evaluation of the spectral luminosity of the accretion disk as a function of $h\nu/kT_*$, i.e., as a function of frequency. In both figures, the solid curves represent the case of a static BH without DM and the dashed curves show the presence of DM with different $\rho_0^* = \rho_0/(10^{-5}\,\mathrm{au}^{-2})$. Here we have used the exponential density profile only.

In this regard, we show in Figure 3 (right panel) that the spectral luminosity is smaller for smaller frequencies, and the spectral luminosity is larger for larger frequencies, with respect to the Schwarzschild case. The results are consistent with the ones obtained in Boshkayev et al. (2020) and Kurmanov et al. (2022), where we investigated the cases of isotropic and anisotropic

Table 1
Physical Parameters of Test Particles and DM with the Exponential Sphere Density Profile

ρ_0^*	P_b, (10^{-8}au^{-2}) with Isotropic Pressures	$r_{\rm ISCO}$, (AU) with Isotropic Pressures	$r_{\rm ISCO}$, (AU) with Tangential Pressure	r_s, (AU)	$M_{\rm DM}(r_s)$, ($10^{-2}M_{\rm BH}$)
0.5	2.082	29.213	29.141	221.261	1.249
1.0	4.187	28.751	28.679	233.459	2.498
1.5	6.313	28.365	28.218	243.154	3.747
2.0	8.462	27.954	27.764	253.001	4.996

Note. The first column shows the values of the central density given by $\rho_0 = \rho_0^* \times 10^{-5}$ au^{-2}; the second column is the value of the pressure at $r = r_b$ in the presence of isotropic pressures; the third column is the radius of the innermost stable circular orbit $r_{\rm ISCO}$ in the presence of isotropic pressures; the fourth column is $r_{\rm ISCO}$ in the presence of tangential pressures only; the fifth column is the surface radius of the DM envelope in the presence of isotropic pressures, which we also adopt for the tangential pressure, for comparison; and the sixth column is the DM mass in units of BH mass.

Table 2
Physical Parameters of Test Particles and DM Analogous to Table 1, but with the Burkert Density Profile

ρ_0^*	P_b, (10^{-8}au^{-2}) with Isotropic Pressures	$r_{\rm ISCO}$, (AU) with Isotropic Pressures	$r_{\rm ISCO}$, (AU) with Tangential Pressure	r_s, (AU)	$M_{\rm DM}(r_s)$, ($10^{-2}M_{\rm BH}$)
0.5	1.208	29.403	29.364	221.208	2.264
1.0	2.425	29.119	29.143	225.571	4.577
1.5	3.652	28.981	28.917	227.278	6.893
2.0	4.887	28.745	28.693	230.121	9.252

pressures. This suggests that the behavior of the spectral luminosity is affected by the presence of DM in the surroundings of the BH, and that the specifics of the matter model do not substantially alter the results.

In fact, one can always construct plots similar to Figures 1–3 using different DM density profiles, like, for instance, the Burkert profile. However, no substantial difference will appear. In order to better quantify the impact of tangential pressure, we present in Tables 1–2 some numerical values for the DM envelope, using both the exponential sphere and Burkert density profiles, and, for completeness, we compare with the case where the same density profile is used for a DM envelope with isotropic pressures.

In Table 1, we present the exponential sphere density profile, while in Table 2, we present the Burkert profile, for comparison. For both profiles, we considered two cases: with isotropic pressures and with tangential pressure only. In the case of the isotropic pressures, one should solve the Tolman–Oppenheimer–Volkoff (TOV) set of equations, in accordance with what was done in Boshkayev et al. (2020). In the case of the tangential pressure, the TOV equations become Equation (9b), in accordance with Florides (1974). Since the tangential pressure is defined via Equations (8a) and (8b), it is obvious that the pressure here is solely given by the density and mass profiles. Also, since there is no need to impose vanishing pressure at the boundary of the surface radius of the DM envelope in the presence of only tangential pressure, r_s is a free parameter.

In order to compare the DM content in the presence of tangential pressure with the case of isotropic pressures, we adopted the same value of r_s for both. Hence, with the same r_s, both cases obviously yield the same mass as shown in the sixth columns of Tables 1 and 2, but slight differences may appear in the location of $r_{\rm ISCO}$, thus influencing the accretion disk's spectrum. However, one can see that, all other things being equal, the values of $r_{\rm ISCO}$ in the two cases are comparable.

5. Conclusions

Spherical matter distributions supported solely by tangential pressures may be used to describe clusters of counterrotating particles and have been used in models of relativistic compact objects for a long time (Kumar Datta 1970; Florides 1974). The early studies of the so-called "Einstein cluster" were mostly aimed at classifying the possible kinds of motion and understanding its relation to the Newtonian case. More recent studies, such as Magli (1997) and Magli (1998), considered dynamical scenarios and gravitational collapse, which may lead to the formation of naked singularities. In Joshi et al. (2011), the "Einstein cluster" was considered as the limiting case of a collapsing cloud, and its observable properties were considered in Joshi et al. (2014). Those models are somewhat related to our current study, since they represent a DM compact object without the presence of a BH. The properties of such objects were further investigated in Joshi et al. (2020). Other authors have considered the "Einstein cluster" as a candidate for DM near the galactic center, most notably Böhmer & Harko (2007) and, more recently, Igata et al. (2022). It has also recently been suggested that the existence of matter field configurations described by an extension of the Einstein cluster model could bear an observable signature in the gravitational-wave signal of binary mergers (Cardoso et al. 2022).

In this paper, we have considered the circular motion of test particles in the field of a static BH surrounded by a DM distribution of counterrotating particles described by the "Einstein cluster" metric. We have computed the accretion disk luminosity spectrum and compared the numerical results with previous works that considered DM envelopes with isotropic and anisotropic pressures. We have showed that the presence of the DM envelope enhances the accretion disk's luminosity.

The results that we have obtained from the tangential pressure picture turned out to be similar to our previous findings where we considered isotropic pressures, such as, for example, Boshkayev et al. (2020). The main differences appear in the value for $r_{\rm ISCO}$ and the value of the total DM mass, which depends on the adopted density profile and its outer boundary (which is free to choose in the tangential pressure case). By putting together the results from this work and those from Boshkayev et al. (2020), we can conclude that the dominant factor in determining the spectral luminosity of the accretion disk is the presence of a DM envelope, regardless of the model chosen for the DM itself.

On one hand, the fact that different fluid models produce similar effects can be considered to be good, since if the predictions were strongly dependent on the type of fluid, it would become more difficult to test such models against other possibilities, such as BH mimickers or compact objects in alternative theories. Noticing that there is consistency in the outcomes regardless of the choice of fluids gives confidence that the hypothesis of the existence of a DM cloud surrounding these objects may be testable in the future. On the other hand, the fact that different DM fluids produce similar accretion disk spectra implies that distinguishing the types of fluids from these observations may be practically difficult, or even impossible. In turn, this means that testing the properties of the DM particles may not be possible. However, we cannot exclude the possibility that the other kinds of observations that are becoming available today, like the motion of the stars near the Milky Way's core and images of the shadows of supermassive BH candidates (Event Horizon Telescope Collaboration et al. 2019), will allow to distinguish the effects of different DM fluid models in the future.

While the present work offers only a qualitative picture for a static spacetime, future efforts will take into account more accurate models of the galaxy, including angular momentum and adopting known observational bounds for the various free parameters of the model. In turn, this may allow us to put constraints on the DM distribution near galactic centers and the properties of central supermassive compact objects.

The authors warmly thank R. D'Agostino and R. Giambò for fruitful discussions on the topics of this work. K.B., T.K., Ye. K., and O.L. acknowledge the Ministry of Education and Science of the Republic of Kazakhstan, grant No. IRN AP08052311. D.M. acknowledges support from Nazarbayev University Faculty Development Competitive Research grant No. 11022021FD2926.

Appendix
Derivations of the Field Equations

Here, we show the derivations of the field equations for a static and spherically symmetric matter distribution with vanishing radial pressures, following Florides (1974). We start with the Einstein field equations, given in the form

$$Q^{\alpha}_{\beta} = G^{\alpha}_{\beta} - kT^{\alpha}_{\beta} = 0, \tag{A1}$$

where G^{α}_{β} is the Einstein tensor, T^{α}_{β} is the energy–momentum tensor, $k = 8\pi$, and α, β=0, 1, 2, 3, with the same geometric units, $G = c = 1$, adopted throughout the paper. To describe the "Einstein cluster," one can take the following components of the energy–momentum tensor:

$$T^0_0 = \rho(r), \quad T^1_1 = 0, \quad T^2_2 = T^3_3 = -P_\theta(r), \tag{A2}$$

where the radial pressure is assumed to be zero. The tangential pressure P_θ must then be found from the field equations with the line element given by Equation (1). We get

$$Q^0_0 = \frac{1}{r^2} - \frac{e^{-\Lambda}}{r^2}(1 - r\Lambda') - kT^0_0 = 0, \tag{A3}$$

$$Q^1_1 = \frac{1}{r^2} - \frac{e^{-\Lambda}}{r^2}(1 + rN') - kT^1_1 = 0, \tag{A4}$$

$$Q^A_B = \frac{e^{-\Lambda}}{2}\left\{\left(\frac{1}{r} + \frac{N'}{2}\right)(\Lambda' - N') - N''\right\}\delta^A_B - kT^A_B = 0, \tag{A5}$$

where A and B refer to components 2 and 3, while prime denotes derivation with respect to r. Obviously, Equation (A3) integrates to give Equation (9a), while Equation (A4) yields Equation (9b).

Now the expressions for Λ' and N' from Equations (A3) and (A4) must be plugged into Equation (A5) to determine T^A_B. As a result, we obtain the tangential pressure as a function of the density profile as

$$T^2_2 = T^3_3 = -P_\theta = -\frac{\rho(r)M(r)}{2(r - 2M(r))}. \tag{A6}$$

It should be mentioned that in the presence of isotropic pressures, one obtains the usual set of TOV equations.

ORCID iDs

K. Boshkayev https://orcid.org/0000-0002-1385-270X
D. Malafarina https://orcid.org/0000-0002-8100-8797

References

Argüelles, C. R., Krut, A., Rueda, J. A., & Ruffini, R. 2018, PDU, 21, 82
Argüelles, C. R., Krut, A., Rueda, J. A., & Ruffini, R. 2019, PDU, 24, 100278
Biretta, J. A., Junor, W., & Livio, M. 2002, NewAR, 46, 239
Böhmer, C. G., & Harko, T. 2007, MNRAS, 379, 393
Bondi, H. 1971, GReGr, 2, 321
Boshkayev, K., D'Agostino, R., & Luongo, O. 2019, EPJC, 79, 332
Boshkayev, K., Idrissov, A., Luongo, O., & Malafarina, D. 2020, MNRAS, 496, 1115
Boshkayev, K., Konysbayev, T., Kurmanov, E., et al. 2021a, MNRAS, 508, 1543
Boshkayev, K., Konysbayev, T., Luongo, O., Muccino, M., & Pace, F. 2021b, PhRvD, 104, 023520
Boshkayev, K., & Malafarina, D. 2019, MNRAS, 484, 3325
Burkert, A. 1995, ApJL, 447, L25
Capozziello, S., D'Agostino, R., & Luongo, O. 2018, PDU, 20, 1
Capozziello, S., D'Agostino, R., & Luongo, O. 2019, IJMPD, 28, 1930016
Cardoso, V., Destounis, K., Duque, F., Macedo, R. P., & Maselli, A. 2022, PhRvD, 105, L061501
Copeland, E. J., Sami, M., & Tsujikawa, S. 2006, IJMPD, 15, 1753
D'Agostino, R., Luongo, O., & Muccino, M. 2022, arXiv:2204.02190
Davis, B. L., Graham, A. W., & Cameron, E. 2019, ApJ, 873, 85
Dokuchaev, V. I., & Nazarova, N. O. 2019, Univ, 5, 183
Einstein, A. 1939, AnMat, 40, 922
Event Horizon Telescope Collaboration, Akiyama, K., Alberdi, A., et al. 2019, ApJL, 875, L1
Faber, T., & Visser, M. 2006, MNRAS, 372, 136
Florides, P. S. 1974, RSPSA, 337, 529
Harada, T., Iguchi, H., & Nakao, K.-I. 1998, PhRvD, 58, 041502
Igata, T., Harada, T., Saida, H., & Takamori, Y. 2022, arXiv:2202.00202
Israel, W. 1966, NCimB, 44, 1
Israel, W. 1967, NCimB, 48, 463
Jhingan, S., & Magli, G. 2000, PhRvD, 61, 124006
Joshi, A. B., Dey, D., Joshi, P. S., & Bambhaniya, P. 2020, PhRvD, 102, 024022
Joshi, P. S., Malafarina, D., & Narayan, R. 2011, CQGra, 28, 235018
Joshi, P. S., Malafarina, D., & Narayan, R. 2014, CQGra, 31, 015002
Kormendy, J., & Ho, L. C. 2013, ARA&A, 51, 511
Kumar Datta, B. 1970, GReGr, 1, 19
Kurmanov, E., Boshkayev, K., Giambò, R., et al. 2022, ApJ, 925, 210
Luongo, O., & Muccino, M. 2018, PhRvD, 98, 103520
Magli, G. 1997, CQGra, 14, 1937
Magli, G. 1998, CQGra, 15, 3215
Navarro, J. F., Frenk, C. S., & White, S. D. M. 1996, ApJ, 462, 563
Novikov, I. D., & Thorne, K. S. 1973, in Black Holes (Les Astres Occlus), ed. C. De Witt & B. De Witt (New York: Gordon and Breach), 343
Page, D. N., & Thorne, K. S. 1974, ApJ, 191, 499
Pastorini, G., Marconi, A., Capetti, A., et al. 2007, A&A, 469, 405
Sofue, Y. 2013, PASJ, 65, 118
Volonteri, M. 2010, A&ARv, 18, 279